

Love wave amplitude decay from rotational ground motions

Bryant Chow^{1,2}, Joachim Wassermann,¹ Bernhard S.A. Schuberth^{1,3},
Céline Hadzioannou,^{1,3} Stefanie Donner^{1,4} and Heiner Igel¹

¹Department of Earth and Environmental Sciences, Ludwig-Maximilians-Universität München, Theresienstraße 41, D-80333 Munich, Germany. E-mail: bryant.chow@lmu.de

²Victoria University of Wellington, School of Geography, Environment and Earth Sciences, Cotton Building, Gate 7 Kelburn Parade, Wellington 6012, New Zealand

³Geophysics, Center for Earth System Research and Sustainability (CEN), Universität Hamburg, D-20146 Hamburg, Germany

⁴Federal Institute for Geosciences and Natural Resources, Stilleweg 2, D-30655 Hannover, Germany

Accepted 2019 May 8. Received 2019 May 5; in original form 2018 August 7

SUMMARY

The broad-band surface wave magnitude equation assigns magnitudes based on source-receiver distance and peak surface wave amplitude. It is standard practice to use the vertical component of peak ground velocity to determine magnitude, such that only contributions from the vertical motion of Rayleigh waves are present in the surface wave train. With the advent of rotational ground motion observations from instruments such as ring laser gyroscopes, it is possible to measure rotational ground motions about three orthogonal axes. For surface waves, observations of rotations about the vertical axis are theoretically only sensitive to the transverse nature of Love waves, unaffected by either component of Rayleigh waves. We use this concept to separate and study the amplitude information of surface waves independently. With a large database of recorded seismic waveforms for colocated translations and rotations, collected in Wettzell, Germany, we empirically define magnitude scale attenuation constants as a method for quantifying amplitude decay. Through this differential analysis, we determine a necessity for separate surface wave magnitude equations through measurements of translations and rotations. Synthetic seismograms were concurrently produced using an open-source spectral-element wave propagation code, for comparisons against observations. Although synthetically derived amplitude decays agree for translations, they do not accurately predict the decay found for rotations. Synthetics also overpredict amplitudes for both rotations and translations. Results from observations imply that rotation amplitudes decay faster over distance with respect to velocity amplitudes, and that the current surface wave magnitude equation is insufficient for predicting observed translation and rotation amplitudes. We attribute variations in amplitude decay characteristics to the different effects of attenuation on Love and Rayleigh waves, with potential influence from local velocity structure and scattering effects. The lack of agreement in synthetics is attributed to the insufficiency of synthetic attenuation and velocity structure to replicate the effects seen in observations.

Key words: Rotational seismology; Seismic attenuation; Surface waves and free oscillations.

1 INTRODUCTION

For over a decade, the application of ring laser gyroscope technology to the field of seismology has allowed for near-continuous, direct measurements of rotational ground motions. An ever growing number of observations from seismic events of varying size, distance and source mechanism, have been collected in an expansive catalogue of waveform recordings for both direct rotation, and colocated translation measurements. Some examples of previous work on this unique waveform data set include phase comparisons of translations and rotations with estimations of horizontal phase

velocities (Igel *et al.* 2005), automatic standardized processing of rotation and translation data (Salvermoser *et al.* 2017), and variations of surface wave energy in oceanic microseisms (Tanimoto *et al.* 2016).

In this paper, we aim to characterize and understand the differences in amplitude decay behaviour of rotational and translational ground motion. To accomplish this, we make use of a catalogue of earthquake observations from an observatory based ring laser gyroscope, and a colocated broad-band seismometer. By processing rotation and translation observations in a near identical manner, we differentially compare amplitude measurements over a range of

epicentral distances and azimuths. Through this comparative study, we seek to better understand decay characteristics of surface waves, with emphasis towards vertical component rotation measurements and their connection to Love waves.

This study builds on results previously shown by Igel *et al.* (2007), who explored whether observed peak amplitudes of rotation matched with expected amplitude values given by the surface wave magnitude equation; they found good agreement for a modified version of the equation, but were limited to a small number of events. We attempt to readdress the question by determining our own magnitude scales through estimation of attenuation constants, with which we quantify decay characteristics of rotations and translations. We concurrently perform global 3-D synthetic simulations with a spectral-element based wave propagation code (Specfem3D Globe), in order to provide a comparative set of synthetic observations. In comparing estimated magnitude scales and expected amplitudes, we are able to make quantitative statements on surface wave amplitude decay. We also seek to provide station-specific, Love wave sensitive, rotation-based magnitude scale equations, that allow for quick approximation of expected rotation amplitudes from teleseismic surface waves.

2 ROTATIONAL GROUND MOTIONS

In continuum mechanics, rotation defines displacement due to the skew-symmetric portion of the strain tensor, and is required to fully describe displacement of a point relative to neighboring points, alongside rigid body translation and the symmetric portion of the strain tensor (Aki & Richards 2002; Igel *et al.* 2005). Standard seismological practice makes extensive use of translation, however these measurements are intermixed with rotation signals, and therefore only provide an approximation of motion at a point. Rotational ground motions induced by seismic events can currently be observed through direct measurement, and through array analysis of translation sensors (e.g. Spudich *et al.* 1995; Donner *et al.* 2017).

Observations for this study were recorded by the Großering (G-ring; BW.RLAS, Schreiber *et al.* 2006a,b), a 4 m x 4 m helium–neon ring laser gyroscope, located at the Geodetic Fundamentalstation in Wettzell, Germany (49.144°N, 12.87°E). The G-ring operates on the principle of Sagnac interferometry (Stedman 1997), which relates interference of counter-propagating light beams to absolute rotation rate through,

$$\delta f = \frac{4A}{\lambda P} \mathbf{n} \cdot \boldsymbol{\Omega}, \quad (1)$$

where an observable beat frequency δf [Hz] is related to absolute rotation rate $\boldsymbol{\Omega}$ [rad s^{-1}], with constants given by instrument area A , perimeter P and operating light wavelength λ .

It is important to note that given stable instrument geometry and lasing, changes to the beat frequency δf , can only be introduced through changes to the inner product of the plane normal \mathbf{n} with the rotation rate direction $\hat{\boldsymbol{\Omega}}$ (e.g. through instrumental tilt), and through externally induced rotations (e.g. the passing of seismic waves). It has been shown that changes to the inner product as produced by tilt are one to two orders of magnitude smaller than rotations produced by seismic waves (McLeod *et al.* 1998; Schreiber *et al.* 2006a,b), which provides the unique benefit that instruments operating on Sagnac interferometry are theoretically insensitive to translations, an important feature that we take advantage of in this work.

2.1 Phase velocity relation

It has been shown that for a transversely polarized plane wave, the amplitudes of vertical rotation rate Ω_z and transverse acceleration \ddot{u}_t can be related by

$$\frac{\ddot{u}_t}{\Omega_z} = -2c, \quad (2)$$

where c [m s^{-1}] represents an apparent horizontal phase velocity (e.g. Igel *et al.* 2005). Given a sufficient source–receiver distance to allow for a plane wave assumption, eq. (2) states that rotations show similar sensitivity to seismic waves as the transverse component of translation; in teleseismic waveforms, transverse translation is sensitive to SH and Love waves. Eq. (2) also shows that waveforms of transverse acceleration and vertical rotation rate should be in phase, with oppositely polarized amplitudes scaled by local phase velocities. Phase matching can be seen in Fig. 1, which shows two superimposed traces of rotation rate and transverse acceleration filtered at 10–60 s for an M_{wc} 6.67 event near Japan (see Table 1). For both observations (top panel) and synthetics (bottom panel), we can see that rotation rate and transverse acceleration are near-identical in the surface wave train.

2.2 Peak correlation coefficient

Correlations are a useful measure of similarity between two signals. For colocated measurements of vertical rotation rate and transverse acceleration, high values (>0.9) of zero-lag correlations can be obtained in time windows centered around S -wave or surface wave arrivals (Igel *et al.* 2007). Zero-lag correlation coefficients are routinely computed for events measured by the G-ring (Salvermoser *et al.* 2017), and are used in this study as a filter to remove events that exhibit low signal-to-noise ratios, or dissimilar waveforms, which may arise due to breakdown of the plane wave assumption, or non-physical effects such as instrument problems. The largest correlation coefficient obtained for a seismogram is labelled the peak correlation coefficient (PCC), and is used as a representation of data quality. To ensure that we are using quality waveforms in our analysis, we calculate correlations of vertical rotation rate and transverse acceleration, and only use waveforms which fall within the bounds $0.7 \leq \text{PCC} \leq 1.0$.

3 SURFACE WAVE MAGNITUDE SCALES

Amplitude based magnitude scales provide empirically derived relationships between maximum trace amplitudes and source–receiver distances. Magnitude scales offer quick estimates of relative sizes for seismic events in a simple, standard manner. A magnitude equation for teleseismic surface waves was first developed by Gutenberg & Richter (1936), and was based on maximum recorded horizontal ground displacements, at a period of 20 s, where traditional seismograms showed their most prominent surface wave signals (Aki & Richards 2002). Displacement was later replaced by maximum ground particle velocity $V_{\text{max}}/2\pi = (A/T)_{\text{max}}$ (Soloviev 1955), because it more closely relates to seismic energy, and better accounts for the wide range of periods at which surface waves exhibit their largest amplitudes (Bormann 2012); the quantity 2π is used as a correction term for velocity magnification relative to the displacement term. The standard surface wave magnitude equation, known as the Prague (or Moscow–Prague) formula, was derived using globally

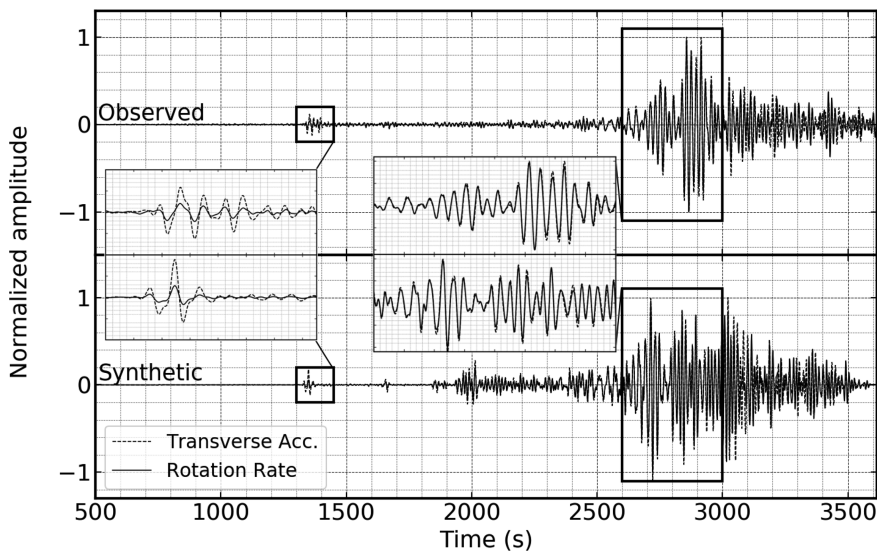


Figure 1. Phase matching between observed (top panel) and synthetic (bottom panel) vertical rotation rate and transverse acceleration, for an M_{wc} 6.67 event near Japan (Table 1). Waveforms bandpass filtered at 10–60 s. Insets show zoomed-in portions highlighted by the boxes around each waveform.

Table 1. Events used as sources in synthetic simulations. Event information taken from the GCMT catalogue.

	Date	Time (UTC)	Lat (°)	Lon (°)	Depth (km)	M_{wc}	Flinn-Engdahl Region
1	2011-09-16	19:26:41	40.27	142.78	35.0	6.67	Off East Coast Of Honshu, Japan
2	2013-04-19	19:58:40	49.97	157.65	15.0	6.06	East Of Kuril Islands
3	2015-09-13	08:14:12	25.14	-109.43	10.0	6.6	Gulf Of California
4	2016-01-25	04:22:02	35.65	-3.68	12.0	6.38	Strait Of Gibraltar

averaged attenuation functions, and has the form

$$M_s = \log_{10}(A/T)_{\max} + 1.66 \cdot \log_{10}(\Delta) + 3.3, \quad (3)$$

where A [μm] is the maximum ground displacement, T [s] is the period where maximum particle velocity $(A/T)_{\max}$ [$\mu\text{m s}^{-1}$] occurs, and Δ [$^\circ$] is the epicentral distance (Karnik *et al.* 1962; Vaněk *et al.* 1962). Despite the term T in eq. (3), the Prague formula is defined for periods between 18 and 22 s, following the original definition by Gutenberg & Richter (1936).

A modified Prague formula, more compatible with modern broad-band seismometers, was proposed by the International Association of Seismology and Physics of Earth's Interior (IASPEI) (Bormann & Dewey 2013). The broad-band surface wave magnitude equation is given as

$$M_s^{\text{BB}} = \log_{10}(V_{\max}/2\pi) + B \cdot \log_{10}(\Delta) + C, \quad (4)$$

where V_{\max} [nm s^{-1}] is the peak surface wave amplitude for a vertical-component seismogram proportional to velocity. The two attenuation constants $B = 1.66$ and $C = 0.3$, correspond to the slope and intercept, respectively. A period range of $3 \text{ s} \leq T \leq 60 \text{ s}$, ensures that peak surface wave energy at a wide range of periods is captured. Epicentral distances range $2^\circ \leq \Delta \leq 160^\circ$, and only shallow focus earthquakes ($z \leq 60 \text{ km}$) are considered, as eq. (4) has no depth dependent correction term (Bormann & Dewey 2013).

Amplitude based magnitude scales are empirically derived and therefore not linked to physical sources. They also incorrectly use logarithms (quantities within logarithms should be dimensionless), and exhibit saturation effects at large magnitudes (Stein & Wysession 2009). Eq. (3) has also been shown to exhibit distance biases, requiring alterations to the attenuation functions (e.g. Herak & Herak 1993; Ambraseys & Free 1997). Regardless, M_s values are still published and cited regularly (e.g. Ekström *et al.* 2012), and

more modern quantities such as the moment magnitude M_w , were derived to roughly agree with M_s . Additionally, for historical events, M_s may be the only comparative measure to modern earthquakes, which makes it a useful quantity despite underlying inaccuracies. We therefore use eq. (4) as a template for estimating attenuation constants in order to compare amplitude decay characteristics of rotations and translations, while acknowledging the above mentioned limitations of magnitude scales.

3.1 Instrumental proxies for Love and Rayleigh waves

The broad-band surface wave magnitude scale takes amplitudes measured on the vertical component to isolate vertical motions of Rayleigh waves; vector sums of horizontal components are influenced by Love and Rayleigh waves. In the same vein, velocity measured on the transverse component should only show sensitivity to Love waves. It is not common practice to use radial or transverse components in calculating magnitude due to the necessity of rotating horizontal components to the correct azimuth. Vertical rotation measurements are however, insensitive to translations, and should only be sensitive to Love waves in the surface wave train. In this study, we use instruments as physical wave filters, in order to study individual sections of the surface wave train. By comparing the vertical and transverse components of translations, to the vertical component of rotation, we can analyse the influences of Love waves and Rayleigh waves separately.

In order to compare translations and rotations using derived magnitude scales, a rotation parameter complementary to velocity is required in eq. (4). Eq. (2) relates rotation rates Ω with accelerations \ddot{u} , so it would make sense to use rotation ω as a comparative variable for velocity \dot{u} (by time integration of both variables). We present

here observations of both rotations and rotation rates, noting that rotation rate is the direct measurement from the G-ring.

3.2 Derived magnitude scales

We adhere to the standard procedures for magnitude calculation provided by IASPEI (Bormann & Dewey 2013) as a stencil for estimating attenuation constants. We in turn use these constants as a tool for comparing amplitude decay of different measured observables. We rearrange eq. (4) to give

$$B \cdot \log_{10}(\Delta) + C = M - \log_{10}(X/2\pi), \quad (5)$$

where vertical velocity V_{\max} in eq. (4) has been replaced with a general peak amplitude measurement X . For simplicity we leave the quantity 2π and do not alter X for measurements of rotation. If we have N observations of amplitudes X_n , and distances Δ_n , we can formulate eq. (5) as the matrix–vector equation

$$\begin{pmatrix} \log_{10}(\Delta_1) & 1 \\ \log_{10}(\Delta_2) & 1 \\ \vdots & \vdots \\ \log_{10}(\Delta_N) & 1 \end{pmatrix} \begin{pmatrix} B \\ C \end{pmatrix} = \begin{pmatrix} M_1 - \log_{10}(X_1/2\pi) \\ M_2 - \log_{10}(X_2/2\pi) \\ \vdots \\ M_N - \log_{10}(X_N/2\pi) \end{pmatrix}. \quad (6)$$

Using a simple linear regression, described in Section 4.2, we can solve for the vector containing unknown attenuation constants B and C , thereby deriving dimensionless quantities to compare amplitude–distance relationships of various observables.

3.3 Attenuation constants

The magnitude equation describes a logarithmic decay, where B represents the slope and C the intercept. Due to the logarithmic nature of the scale, and the fact that amplitudes can be expressed in arbitrary orders of magnitude, the value of C is relative; for example, converting velocities from $\mu\text{m s}^{-1}$ to nm s^{-1} will change the value of C by 3. To see how changes in B relate to changes in expected amplitudes, we allow the value of B to vary and compare expected amplitudes estimated from the inverse of the magnitude equation. Fig. 2 shows that small changes to B ($\Delta B = 0.25$), for a fixed value of C , result in a factor of two, to a factor of four difference in expected amplitudes, depending on epicentral distance. In this study, velocity amplitudes on the order of nm s^{-1} and rotation amplitudes on the order of prad s^{-1} relate to values of C ranging from 1.0 to 2.0. Results indicate that B ranges from roughly 1.0 to 2.0.

4 METHODS

4.1 Data processing

Events were processed in a similar fashion as in Salvermoser *et al.* (2017). Raw, continuous, translation data in north, east and vertical components, as well as vertical rotation rate data, was fetched based on event origin time. Instrument response correction produced translation seismograms proportional to units of ground velocity (nm s^{-1}), with a flat response between 120 s and 10 Hz. Epicentral distances (Δ) and theoretical backazimuth values were calculated from source and receiver latitude longitude values. Translations were rotated into the transverse, radial, vertical coordinate system by the appropriate backazimuth. Measurements from ring laser gyroscope instruments do not require frequency dependent instrument correction (Schreiber *et al.* 2006a); a scale factor was

multiplied with the data to retrieve seismograms proportional to rotation rate (nrad s^{-1}), and then time integrated to give seismograms proportional to rotation (nrad).

A bandpass filter was applied to all traces for periods between $3 \text{ s} \leq T \leq 60 \text{ s}$. Peak amplitudes were chosen by finding minimum and maximum trace values and the largest associated peak or trough, respectively. The larger of the two was recorded, alongside associated arrival time and dominant period. Through manual inspection, picked amplitudes that fell outside the surface wave train were removed. An example of peak amplitude picking is shown in Fig. 3, where isolation of surface waves can be seen when comparing vertical velocity to the other three components. A more technical explanation of processing steps is given in the Appendix.

To calculate peak correlations, traces of transverse acceleration and vertical rotation rate were segmented into two minute time windows, in which zero-lag cross correlation was performed. From the entire trace, the maximum correlation value were taken to represent the peak correlation coefficient.

4.2 Linear regression

To quantify amplitude decay, we fit attenuation constants to data using a simple linear regression. To make use of the linear regression method, we assume amplitude and distance are logarithmically related, that distance measurements are error-free and that our amplitude measurements are log-normally distributed, and independent from one another. We assume that the errors in calculated great-circle distances are negligible. After removal of outliers, we assume a log-normal distribution (Fig. A1) for translation and rotation measurements. Residuals between observed and expected amplitudes using our estimated attenuation constants (Fig. A2), show random scatter, implying that a linear regression is suitable for this data set.

Eq. (6) can be expressed in the general form $\mathbf{G}\mathbf{m} = \mathbf{d}$, with unknowns B and C represented in the vector \mathbf{m} . In solving for \mathbf{m} , we create an empirical magnitude scale that best describes the amplitude decay behaviour of our observations. 95 per cent confidence intervals were constructed for each parameter of the vector \mathbf{m} . These were calculated by the equation $\hat{m}_j \pm c\sqrt{\text{var}(\hat{m}_j)}$, where the value of c is given as 1.96 for a confidence level of $\alpha = 0.95$. The confidence level of $\alpha = 0.95$ was chosen as a standard confidence with an acceptable margin of error for this study.

5 EVENT CHOICE

The G-ring has been continuously recording at its current resolution since May, 2009 (e.g. fig. 2 in Hadzioannou *et al.* 2012). Events used in this study span from 1 June 2009 to 1 September 2016. We set our magnitude range at $6 \leq M_s \leq 7$; Shearer (2009) states that moment magnitude ' M_w ' was defined to agree with M_s mainly for events between $M6$ and 8 ', and that 'we should expect M_s to underpredict M_w at both small and large magnitudes.' We set the upper limit $M_s = 7$ to avoid unwanted effects of magnitude saturation, and we take $M_s \approx M_w$ in this range.

An initial earthquake catalogue was retrieved from the Global Centroid Moment Tensor (GCMT) catalogue (Ekström *et al.* 2012), with events filtered by magnitude, source depth and epicentral distance from the G-ring. We impose the restriction that 'derived magnitudes' as given by our magnitude equations, should fall as close to a catalogue-published moment magnitude as possible (that is $M_{\text{derived}} \stackrel{!}{=} M_w$, where we use the symbol $\stackrel{!}{=}$ to mean 'should be

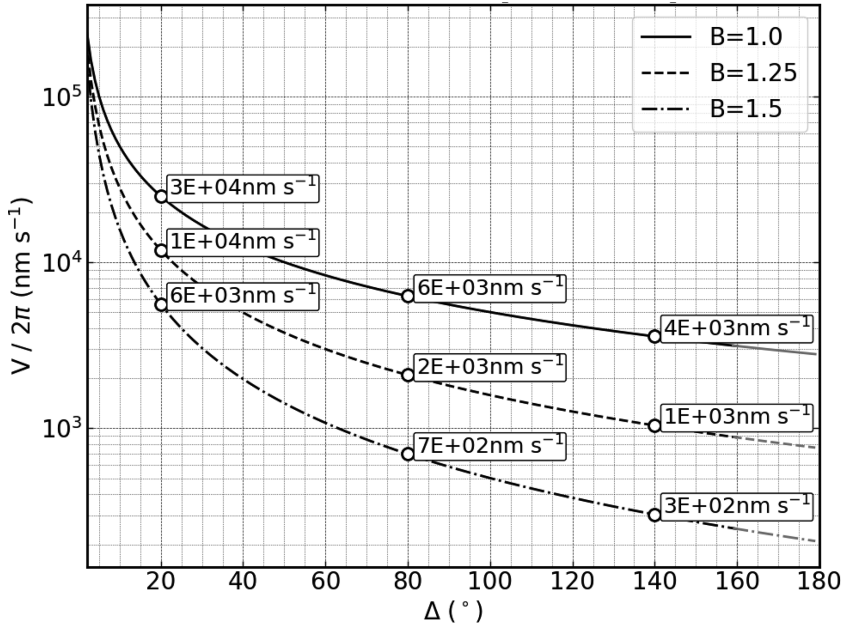


Figure 2. Expected amplitude variations due to changes in the amplitude decay constant B . Varying values of B for $M = 6$ event with a fixed value of $C = 0.3$. Expected amplitude values at epicentral distances Δ , of 20° , 80° and 140° , annotated at corresponding markers. Note y-axis shown in logarithmic scale. At close epicentral distances ($\Delta = 20^\circ$), amplitude variations are roughly a factor of 2 for differences in B of 0.25. At large distances ($\Delta = 140^\circ$), variations are roughly a factor of 4.

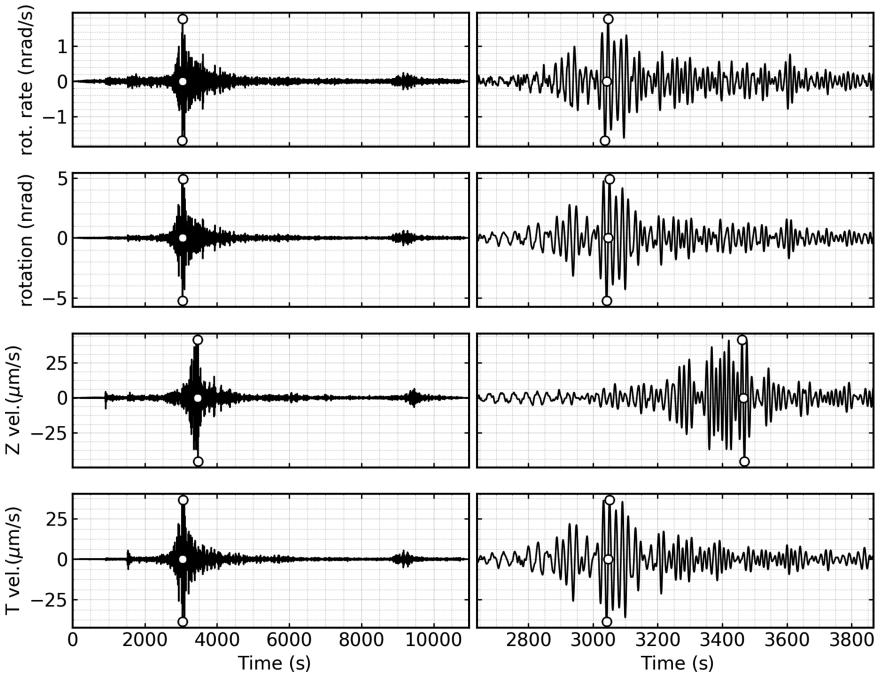


Figure 3. Peak amplitude picking. Left-hand column shows full seismograms for a 2011 M_{wc} 6.67 event (see Table 1). From top to bottom panels: rotation rate, rotation, vertical velocity, transverse velocity. Central dots show zero crossing for the chosen peak to peak amplitude. Outer dots show largest peak and trough values. Right-hand column shows a zoomed in portion, focusing on the surface wave train. Note the difference in arrivals of the Love wave and the later arriving Rayleigh wave.

equal to'). This ensures that our derived scales do not stray far from established scales.

To remove events with low signal-to-noise ratios, zero-lag cross correlations of transverse acceleration and vertical rotation rate were taken in order to calculate peak correlation coefficients. Events were

rejected if their peak correlation coefficient fell below 0.7. A final event catalogue of roughly 200 events was created. An event map is shown in Fig. 4, which highlights the events used in the regression, and events and stations used in deriving synthetic seismograms (Section 6).

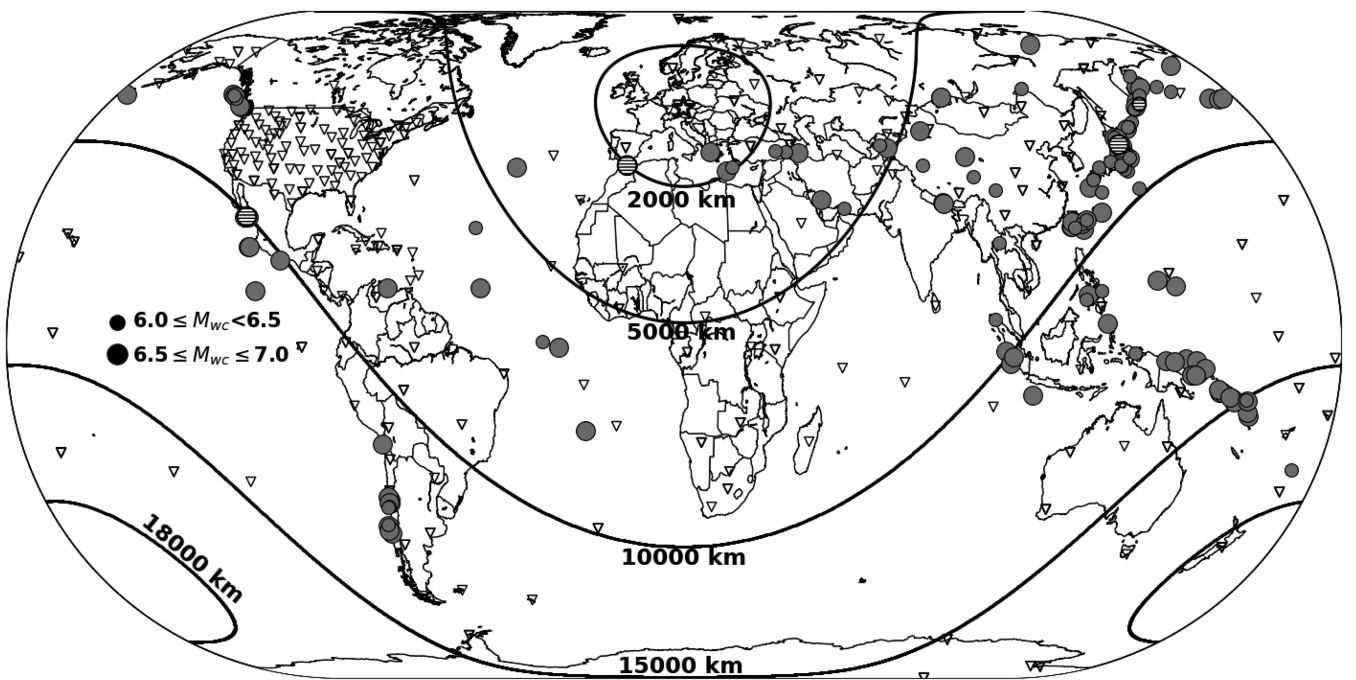


Figure 4. Event map. Circles represent events used for amplitude measurements. Inverted triangles show GSN station locations used in simulations. Hashed circles show events chosen for synthetic seismogram generation (see Table 1). Circle size represents moment magnitude M_{wc} in bins of 0.5. Equidistant lines from Wettzell, Germany, shown in black, with approximate distances annotated. Wettzell marked by a white star ($49.144^{\circ}\text{N}, 12.87^{\circ}\text{E}$).

6 SYNTHETIC SEISMOGRAMS

Rotations are a relatively new observable in seismology, and including measurements from other rotation instruments for comparison would lead to more robust results. However, due to the unique instrumental setup of the G-ring, there are no other comparable data sets to draw comparisons with. It should be mentioned that other rotation instruments exist, and have been used for earthquake analyses (e.g. Donner *et al.* 2017; Sbaa *et al.* 2017), however they lack suitable earthquake catalogues. One possibility for gathering more rotation observations would be through array derived rotations—this option was noted but it proved difficult to identify arrays with optimal station spacing, and sufficient earthquake catalogues. Instead, synthetic rotation and translation waveforms were generated for use in deriving synthetic attenuation constants, which we then compare against our observation-derived constants.

The spectral-element wave propagation code Specfem3D Globe was employed (Komatitsch & Tromp 2002a,b), featuring the 3-D crustal velocity model Crust2.0 (Bassin *et al.* 2000), mantle model S40RTS (Ritsema *et al.* 2011) and 1-D PREM radial attenuation model. Ocean loading, Earth ellipticity, self gravitation and Earth's rotation were included in the simulations, due to their potential influence on long period surface waves. Event locations and moment tensors were taken from four seismic events in our catalogue, chosen based on high peak correlation coefficients, as well as sufficiently varied locations and depths of source–receiver pairings. Table 1 provides more detailed information on the chosen events, which are shown on a map in Fig. 4.

Events were initiated as point sources using GCMT moment tensor inputs. A simulation corner frequency was set to 10 s, and simulations were run for one hour seismogram length. As computational cost is independent of number of stations, more than one hundred real stations were included—locations were taken from Global Seismic Network (GSN) stations, with the addition of the G-ring

and the German observatory station Fürstenfeldbruck ($48.163^{\circ}\text{N}, 11.275^{\circ}\text{E}$).

Outputs of Specfem3D were synthetic translation and rotation waveforms at each station location. The source code was altered to output the curl of the displacement field at each numerical integration point, which was then used to calculate rotation and rotation rate (eq. 2.2, Aki & Richards 2002). Preprocessing followed the same steps as observations, with the addition of convolution of waveforms with triangle source–time–functions of length corresponding to the published centroid half-duration, as well as a bandpass filter with corners at $10\text{ s} \leq T \leq 60\text{ s}$ (as opposed to 3 s and 60 s) due to the computational limitations of the simulation set by the simulation corner.

7 RESULTS

Attenuation constants were estimated for multiple stations and components (Table 2). Comparisons are made between attenuation constants derived for rotations and translations recorded at Wettzell, where the differential nature of this study ensures that source effects are captured in both observables. Estimated attenuation constants are compared against the broad-band surface wave magnitude equation. Path and site effects will, however, have an effect on local attenuation constants not seen in a globally averaged scale; to address this, the same analysis was performed on broad-band translation observations at three other stations: GR.FUR (Fürstenfeldbruck, Germany; $48.163^{\circ}\text{N}, 11.275^{\circ}\text{E}$), II.PFO (Piñon Flats, California, USA; $33.61^{\circ}\text{N}, 116.46^{\circ}\text{W}$) and II.ERM (Erimo, Hokkaido Island, Japan; $42.02^{\circ}\text{N}, 143.16^{\circ}\text{E}$). The same event catalogue was used, though some stations make use of less events due to data availability. Values of B and C for these stations mostly agree with those derived for Wettzell (Table A1). A comparison of translation and rotation attenuation constants for $M = 6.5$ is shown in Fig. 5. Abbreviations

Table 2. Rotation and vertical velocity attenuation constants for eq. (5) ($M = \log_{10}(X/2\pi) + B \cdot \log_{10}(\Delta) + C$). Attenuation constants B and C presented together with 95 per cent confidence intervals. The second to last column gives consideration to the wave type that each instrument component should provide a proxy for, the last column gives the number of samples in the linear regression (BB, Broadband; WET, Wettzell; SYN, synthetic; RLAS, ring laser; ZV, vertical velocity component; RT, vertical rotation component; RR, vertical rotation rate component).

Scale	Label	B	C	Units	Wave	N
IASPEI	$M_{\text{WET}}^{\text{BB}}$	1.66	0.3	nm s^{-1}	Rayleigh	—
Vertical velocity (WET)	$M_{\text{ZV}}^{\text{WET}}$	1.18 ± 0.3	0.95 ± 0.58	nm s^{-1}	Rayleigh	195
Synthetic vertical velocity	$M_{\text{ZV}}^{\text{SYN}}$	1.18 ± 0.09	0.57 ± 0.16	nm s^{-1}	Rayleigh	562
Rotation (RLAS)	$M_{\text{RT}}^{\text{RLAS}}$	1.59 ± 0.41	1.22 ± 0.79	prad	Love	191
Synthetic rotation	$M_{\text{RT}}^{\text{SYN}}$	1.09 ± 0.13	1.57 ± 0.24	prad	Love	569
Rotation rate (RLAS)	$M_{\text{RR}}^{\text{RLAS}}$	1.76 ± 0.39	1.29 ± 0.75	prad s^{-1}	Love	189
Synthetic rotation rate	$M_{\text{RR}}^{\text{SYN}}$	1.13 ± 0.13	1.81 ± 0.24	prad s^{-1}	Love	562

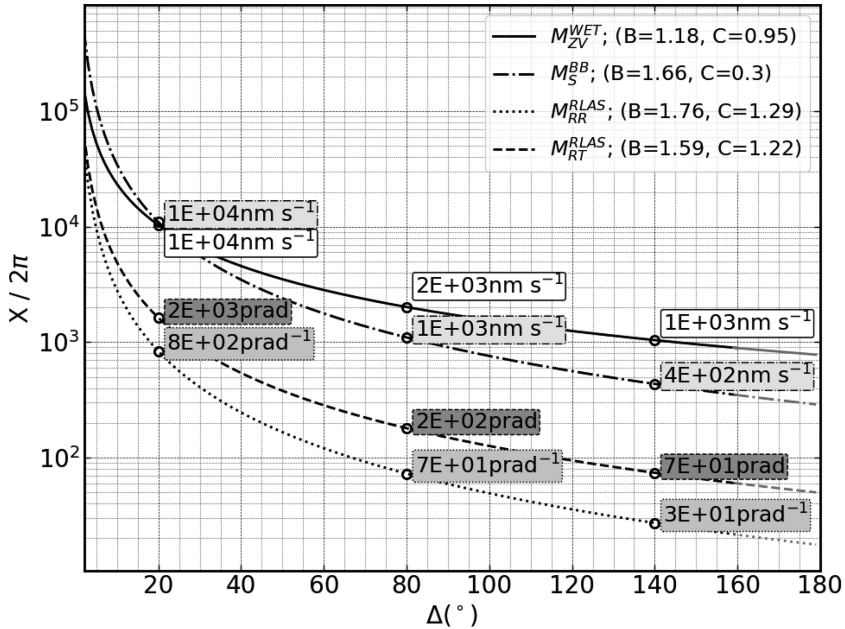


Figure 5. Comparison of amplitude decay from various magnitude scales. For a M6.5 event, vertical velocity $M_{\text{ZV}}^{\text{WET}}$, rotation $M_{\text{RT}}^{\text{RLAS}}$, rotation rate $M_{\text{RR}}^{\text{RLAS}}$ and the broad-band magnitude equation M_{S}^{BB} . Values of B and C for respective magnitude scales provided in legend. Expected amplitude values, grouped by shading, annotated next to markers for 20° , 80° and 140° epicentral distances.

used to denote each site and component are given in the caption of Table 2.

Alongside attenuation constants, expected amplitudes were calculated using the inverse of the magnitude equation by solving eq. (5) for the amplitude X , with given values of B , C , M and Δ . Expected amplitude comparisons for chosen scales are given in Table 3. Through analysis of the attenuation constants and expected amplitudes, we determine that rotation based attenuation constants exhibit faster amplitude decay with distance, compared to velocities on both horizontal and vertical components. Rotation rate and transverse acceleration amplitude decays show similar values, and estimates of transverse velocity amplitude decay fall between estimates for vertical velocities and rotations. Synthetic attenuation constants on the other hand, show little variation between translations and rotations, and also overpredict amplitudes for both translations and rotations, with respect to observations.

7.1 Rotation magnitude scales

Peak rotation amplitudes were scaled to the order of prad or prad s^{-1} to ensure that estimated values of C fell between 1 and 2, for

Table 3. Expected amplitudes from magnitude scales. Values calculated by solving for X in eq. (5), with $M = 6.5$. Rotation and translation based magnitude scales related to labels defined in Table 2. Amplitudes given for epicentral distance values Δ , of 20° , 80° and 140° . Rotation based magnitude scales show faster overall amplitude decay with distance, compared to translation scales. Synthetic magnitude scales overpredict amplitudes compared to observation based magnitude scales.

Scale	$\Delta = 20^\circ$	$\Delta = 80^\circ$	$\Delta = 160^\circ$
$M_{\text{WET}}^{\text{BB}}$	$69.0 \mu\text{m s}^{-1}$	$6.9 \mu\text{m s}^{-1}$	$2.2 \mu\text{m s}^{-1}$
$M_{\text{ZV}}^{\text{WET}}$	$65.0 \mu\text{m s}^{-1}$	$13.0 \mu\text{m s}^{-1}$	$5.6 \mu\text{m s}^{-1}$
$M_{\text{ZV}}^{\text{SYN}}$	$160.0 \mu\text{m s}^{-1}$	$30.0 \mu\text{m s}^{-1}$	$13.0 \mu\text{m s}^{-1}$
$M_{\text{TV}}^{\text{WET}}$	$62.0 \mu\text{m s}^{-1}$	$9.5 \mu\text{m s}^{-1}$	$3.7 \mu\text{m s}^{-1}$
$M_{\text{RR}}^{\text{RLAS}}$	5.2nrad s^{-1}	0.5nrad s^{-1}	0.1nrad s^{-1}
$M_{\text{RR}}^{\text{SYN}}$	10.0nrad s^{-1}	2.2nrad s^{-1}	1.0nrad s^{-1}
$M_{\text{RT}}^{\text{RLAS}}$	10.0nrad	1.1nrad	0.4nrad
$M_{\text{RT}}^{\text{SYN}}$	20.0nrad	4.5nrad	2.1nrad

easier comparison with translation attenuation constants. We present expected amplitudes however, in the more natural units of nrad and nrad s^{-1} . The estimated attenuation constants and 95 per cent confidence intervals for vertical rotation rate measured on the G-ring ($M_{\text{RR}}^{\text{RLAS}}$), are $B = 1.76 \pm 0.39$ and $C = 1.29 \pm 0.75$. Expected

rotation rate amplitude for an $M_{\text{RR}}^{\text{RLAS}}$ 6.5 event at $\Delta = 20^\circ$ is $\sim 5 \text{ nrad s}^{-1}$, and at $\Delta = 160^\circ$ is 0.1 nrad s^{-1} . Rotation measurements were made using peak amplitudes on waveforms equal to the integral of rotation rate. By using measurements of rotation rather than rotation rate, we retrieve slightly different values of B and C . Attenuation constants for rotation on the G-ring ($M_{\text{RT}}^{\text{RLAS}}$) were estimated as $B = 1.59 \pm 0.41$ and $C = 1.22 \pm 0.79$. Excepted rotation amplitude for an $M_{\text{RT}}^{\text{RLAS}}$ 6.5 event at $\Delta = 20^\circ$ is 0.1 nrad , at $\Delta = 160^\circ$ is 0.4 nrad . Rotation rate shows slightly faster amplitude decay with distance, with respect to rotations. Fig. 6 shows a graphical representation of the rotation rate magnitude scale.

7.2 Translation magnitude scales

Attenuation constants for translation magnitude scales give expected amplitudes in units of nm s^{-1} . Here we state expected amplitude values in more natural units of $\mu\text{m s}^{-1}$. At Wettzell, the vertical velocity magnitude scale $M_{\text{ZV}}^{\text{WET}}$, estimates attenuation constants of $B = 1.18 \pm 0.3$ and $C = 0.95 \pm 0.58$. Expected amplitude for $M_{\text{ZV}}^{\text{WET}}$ 6.5 at $\Delta = 20^\circ$ is $65 \mu\text{m s}^{-1}$ and at $\Delta = 160^\circ$ is $\sim 6 \mu\text{m s}^{-1}$. For comparison, expected amplitude from the broad-band surface wave equation M_s^{BB} (eq. (4); $B = 1.66$, $C = 0.3$) for the same magnitude at $\Delta = 20^\circ$ is $\sim 70 \mu\text{m s}^{-1}$, and at $\Delta = 160^\circ$ is $\sim 2 \mu\text{m s}^{-1}$. The broad-band surface wave equation and estimated vertical velocity scale agree at $\Delta = 20^\circ$, but diverge at distance; $M_{\text{ZV}}^{\text{WET}}$ predicts a factor two or three times larger amplitudes compared to M_s^{BB} at large distances. We attribute this to a well documented distance-bias in the correction terms of the original Prague formula (e.g. Herak & Herak 1993; Ambraseys & Free 1997). Proposed attenuation functions that address this distance bias (Table A1) are more similar to the attenuation constants estimated here.

Transverse translation components should only show sensitivity to Love waves. Peak transverse ground velocity at Wettzell was measured, to compare against rotation and vertical velocity. The constants for transverse velocity at Wettzell ($M_{\text{TV}}^{\text{WET}}$) estimates attenuation constants of $B = 1.35 \pm 0.33$ and $C = 0.75 \pm 0.63$, and thus predicts amplitudes for $M_{\text{TV}}^{\text{WET}}$ 6.5 at $\Delta = 20^\circ$ of $\sim 60 \mu\text{m s}^{-1}$, and at $\Delta = 160^\circ \sim 4 \mu\text{m s}^{-1}$. These values are similar to expected amplitudes estimated from vertical velocity.

7.2.1 Magnitude scales for other stations and components

Using the same event catalogue, attenuation constants were calculated for various other stations and components for comparison against rotations and translations measured at Wettzell (Table A1). Attenuation constants were derived for vertical velocity at three other stations, located in Germany, Japan and the U.S.A. These estimated constants agree well with vertical velocity at Wettzell, suggesting that site bias does not play an appreciable role in single station attenuation constant estimation. Transverse velocity attenuation constants were also estimated for Fürstenfeldbruck, and show similar characteristics to transverse velocity at Wettzell. Transverse acceleration attenuation constants were estimated at Wettzell, with amplitude decay showing a similarly large value as rotation rate amplitude decay.

7.3 Synthetic magnitude scales

Synthetic attenuation constants were estimated using peak amplitudes of synthetic waveforms. Magnitude scales were derived in a globally averaged manner where synthetic events were recorded at more than 100 synthetic station locations, providing a more even

sampling of epicentral distances. Interestingly, synthetic attenuation constants do not show the degree of variation that observations do. Synthetic rotation $M_{\text{RT}}^{\text{SYN}}$ estimates attenuation constants $B = 1.09 \pm 0.13$ and $C = 1.57 \pm 0.24$; synthetic rotation rate $M_{\text{RR}}^{\text{SYN}}$ estimates $B = 1.13 \pm 0.13$ and $C = 1.81 \pm 0.24$; synthetic vertical velocity $M_{\text{ZV}}^{\text{SYN}}$ estimates $B = 1.18 \pm 0.09$ and $C = 0.57 \pm 0.16$; synthetic transverse velocity $M_{\text{TV}}^{\text{SYN}}$ estimates $B = 0.94 \pm 0.11$ and $C = 0.94 \pm 0.22$. All synthetic magnitude scales overpredict amplitudes compared to observation based scales, at all distances. Interestingly, all synthetic magnitude scales show effectively the same amount of amplitude decay with distance, which is in contrast to the observed, faster decay of real rotation observations. Table 3 illustrates this discrepancy through differences in expected synthetic amplitude values compared to observations. Fig. 7 shows a graphical representation of the synthetic rotation rate magnitude scale.

7.4 Statistical significance

Residuals between the logarithms of observed and expected amplitudes shows random scatter, confirming that a linear regression is appropriate for this dataset. We calculate 95 per cent confidence intervals for our attenuation constants to determine if our estimated values are significantly different from one another. Due to the large scatter in recorded amplitude values, as well as the uneven spatial sampling of observations, the confidence intervals for estimated, observation-based attenuation constants covers a wide range. Taking values from Table 2, the amplitude decay of rotation with its 95 per cent confidence intervals covers $B_{\text{RT}}^{\text{RLAS}} \pm CI_{95\%} = [1.18, 2.0]$. Conversely, the estimate of amplitude decay for vertical velocity with 95 per cent confidence intervals covers the range $B_{\text{ZV}}^{\text{WET}} \pm CI_{95\%} = [0.88, 1.48]$. The bounds of these confidence intervals overlap, and we therefore cannot claim statistical significance in the difference of our amplitude decay results; we cannot dismiss the possibility that sampling error, sample size and random noise could be the cause for the differences in amplitude decay that we estimate, at the 95 per cent confidence level. A visual comparison of values of B with their 95 per cent confidence intervals is given in Fig. 8.

8 DISCUSSION AND CONCLUSIONS

The long term continuous recordings of rotation and translation waveforms at Wettzell have provided an extensive catalogue of colocated observations to explore four spatial components of seismic signals. In Igel *et al.* (2007), the motivation for addressing amplitude decays was to determine whether or not the commonly used surface wave magnitude equation was a good predictor for rotation amplitudes. We built upon this motivation by investigating how amplitude decay of translations and rotations differ. In this observation based paper, we discover two interesting characteristics of rotation amplitudes: firstly, peak amplitudes of rotation and rotation-rate decay faster with distance compared to colocated measurements of peak velocity, on both horizontal and vertical components. Second, attenuation constants estimated from synthetic rotations do not exhibit the same variation for synthetic rotations as seen in observations.

Many factors can influence amplitude measurements, and each may have varying degrees of influence on rotations and translations. Path attenuation, local velocity structure and scattering are all possible mechanisms for explaining our findings. It is well documented

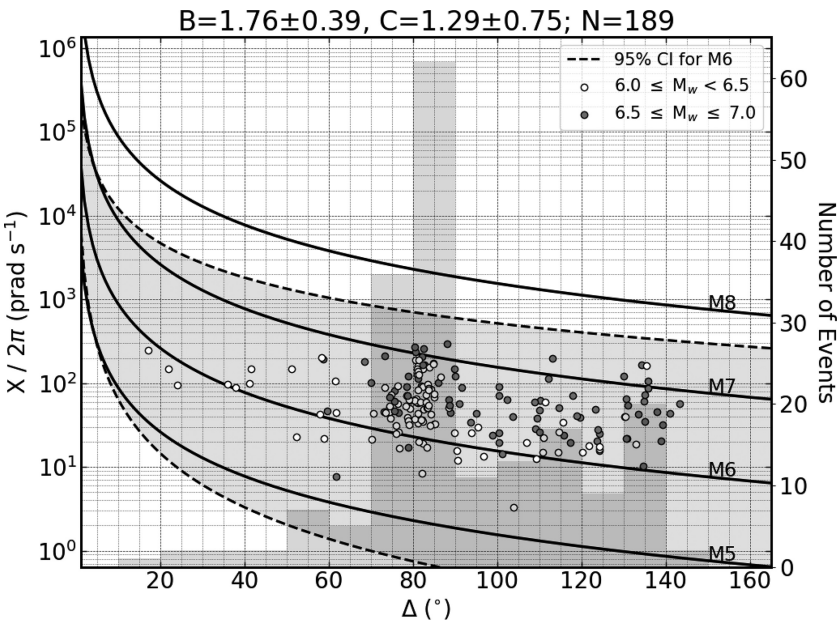


Figure 6. Rotation rate magnitude scale for observations at station BW.RLAS ($B = 1.76 \pm 0.39$, $C = 1.29 \pm 0.75$) following the equation $M = \log_{10}(X/2\pi) + B \cdot \log_{10}(\Delta) + C$. Markers show peak amplitude plotted against epicentral distance for each event. GCMT catalogue-published event magnitude represented by shading of markers, and separated into bins of length 0.5. Eq. (5) plotted by integer values as solid lines with corresponding magnitude annotated at $\Delta = 155^\circ$. 95 per cent confidence interval for M_6 shown by the shaded area, bordered by dashed lines. The number of events for each 10° epicentral distance bin represented by gray bars in the background.

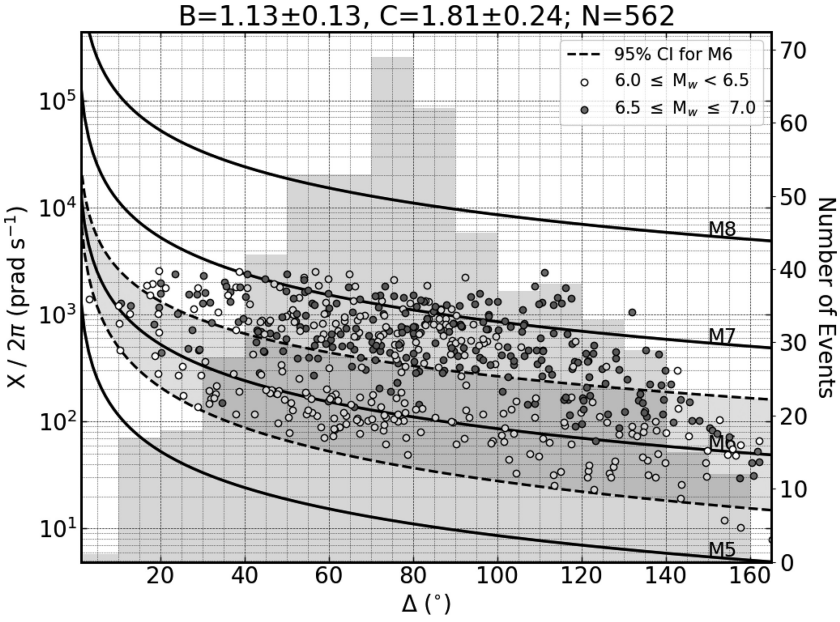


Figure 7. Synthetic rotation rate magnitude scale with $B = 1.13 \pm 0.13$ and $C = 1.81 \pm 0.24$. Same as in Fig. 6, but for amplitudes measured on synthetic waveforms. Amplitudes retrieved from four synthetic events captured at roughly 140 synthetic station locations.

that Love and Rayleigh wave quality factors differ (e.g. Anderson, Ben-Menahem & Archambeau 1965), with Q_{Rayleigh} generally larger than Q_{Love} . This difference implies that Love wave sensitive amplitude measurements should exhibit faster decay with distance compared to Rayleigh wave sensitive measurements, which we observe. Transverse velocity attenuation constants, sensitive to Love waves, estimate slightly larger amplitude decay, though nowhere near the differences with respect to vertical velocities that rotations do; to explain the increased observed amplitude decay of rotations potentially requires further mechanisms.

Local velocity structure will also affect rotation amplitude measurements; as shown in eq. (2), for a plane wave, rotation measurements are tied to amplitudes of transverse acceleration via local velocity structure. The fact that multiple stations in different tectonic regions provide consistent attenuation constants for vertical velocity suggests that local velocity structure may not have a strong effect on Rayleigh wave sensitive measurements. Additionally, attenuation constants derived for measurements of peak transverse acceleration at Wettzell ($M_{\text{TA}}^{\text{WET}}$ in Table A1) shows comparable amplitude decay to vertical rotation rate, implying

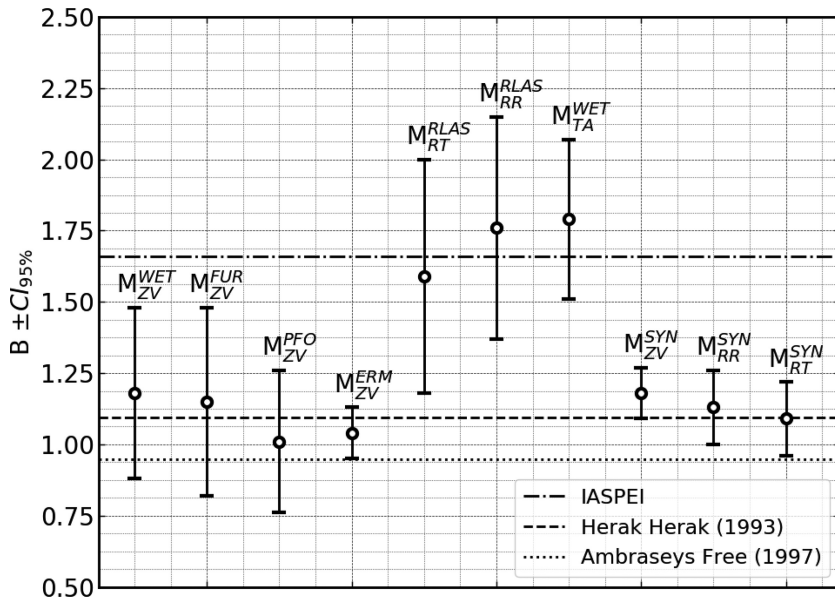


Figure 8. Values of B with 95 per cent confidence intervals for various scales given in Tables 2 and A1. Markers show estimated value of B for respective scales, annotated above. Error bars show the extent of 95 per cent confidence intervals. Values grouped to illustrate that vertical velocity amplitude decay estimates range from values between 1.0 and 1.25, while rotation-based and transverse acceleration amplitude decay estimates lie above 1.5. Fixed values of amplitude decay for various scales published in literature given as horizontal dashed lines.

that local velocity structure does not play a strong role in attenuation constant estimation. However, our methods do not allow us to rule out these effects, nor can we rule out the effects of scattering due to velocity heterogeneities, which may have differing effects on transverse and vertically polarized waves. Future study is required to determine the physical mechanism behind these findings.

We cannot claim statistical significance at the 95 per cent confidence level for our results, and therefore cannot reject the possibility that our estimates are due to insufficient sampling or measurement noise. More samples at epicentral distances not well covered in this study are required to reduce uncertainty in estimates. Additionally, more rotation measurements from other site locations will produce more robust comparisons with translations. However, we argue that the similar, repeat estimates of B for both vertical velocity and transverse velocity at various site locations, and the similarly large values of B for both rotation rate and transverse acceleration (Fig. 8), reinforce our conclusion that amplitude decay estimates are linked to attenuation characteristics, and not to random noise or sampling error. Through the simple lens of attenuation constants, it is difficult to distinguish which mechanisms are responsible for the differences observed in rotation and translation amplitude decays, however we argue that differences in surface wave attenuation characteristics provide the strongest driving mechanism. We ultimately leave this an open question for future study.

Synthetic magnitude scales do not reflect variations of rotation and translation amplitude decay seen in observations, and synthetic amplitudes are overall two or three times larger than those observed. Amplitude attenuation can be attributed to anelastic attenuation, geometrical spreading, diffraction effects (i.e. focusing/defocusing) and scattering (e.g. Stein & Wysession 2009). Using fully 3-D global waveform simulations, we account for geometrical spreading, and ignore the effects of scattering due to a numerically smooth velocity model. The inadequacy of synthetics to predict amplitude decays of observations may arise due to an unrealistic attenuation model,

improper honoring of diffraction effects, or lack of local velocity structure information. Implementation of a 1-D PREM radial attenuation model gives rise to a simplified view of attenuation structure in our simulations, which may lead to overestimated amplitudes. In addition, the crustal and upper mantle models used may not account for realistic diffraction effects, such as defocusing. Finally, because rotations are tied to local velocity structure, a lack of realistic local velocity model provides another possible explanation for why synthetic rotations show almost identical amplitude decay as synthetic velocities. Although utilized in this study, we conclude that a more detailed investigation of synthetic rotations is necessary, and we pose the questions: do spectral-element wave propagation codes accurately model rotational ground motions, as compared to translations? Additionally, would the inclusion of a more detailed local velocity structure model lead to variations of rotation and translation amplitude decay observed in real-world measurements? We believe that these important questions should be addressed in future studies.

The amplitude characteristics of rotational ground motions are a unique study area that has yet to be addressed on similar scales as translational ground motions. Further in-depth studies will be necessary to pinpoint the physical mechanisms controlling rotation decay behaviour and their differences with respect to translations. Among the traits discovered for rotational ground motions, we highlight the ability to instrumentally separate the influences of surface waves as a useful seismological tool, especially in the single-station context (e.g. planetary seismology), where the availability of six-component recordings may help in more robust separation of seismic phases (e.g. Sollberger *et al.* 2017). We emphasize that this unique collection of colocated rotation and translation measurements provides an interesting data set that has not yet been fully explored; this introductory, comparative study of rotations and translations investigates interesting qualities of amplitude decay characteristics, but a wealth of information exists in this expansive collection of colocated recordings.

ACKNOWLEDGEMENTS

This work was made possible by the European Research Council (ERC) Advanced Grant ‘ROMY’ (Rotational Motions in Seismology). This paper benefited immensely from two anonymous reviewers, who helped strengthen and clarify the manuscript. Thanks to Toshiro Tanimoto for references and guidance.

REFERENCES

- Aki, K. & Richards, P.G., 2002. *Quantitative Seismology*, 2nd edn, University Science Books.
- Ambraseys, N. & Free, M., 1997. Surface-wave magnitude calibration for European region earthquakes, *J. Earthq. Eng.*, **1**(01), 1–22.
- Anderson, D.L., Ben-Menahem, A. & Archambeau, C.B., 1965. Attenuation of seismic energy in the upper mantle, *J. geophys. Res.*, **70**(6), 1441–1448.
- Bassin, C., Laske, G. & Masters, G., 2000. The current limits of resolution for surface wave tomography in North America, *EOS, Trans. Am. Geophys. Un.*, **81**(48), F897.
- Beyreuther, M., Barsch, R., Krischer, L., Megies, T., Behr, Y. & Wassermann, J., 2010. ObsPy: a Python toolbox for seismology, *Seismol. Res. Lett.*, **81**(3), 530–533.
- Bormann, P., 2012. *New Manual of Seismological Observatory Practice (NMSOP-2)*, IASPEI, GFZ German Research Centre for Geosciences, Potsdam.
- Bormann, P. & Dewey, J.W., 2013. IS3.3: The new IASPEI standards for determining magnitudes from digital data and their relation to classical magnitudes, in *New Manual of Seismological Observatory Practice (NMSOP2)*, <http://bib.telegrafenberg.de/publizieren/vertrieb/nmsop/>.
- Donner, S. et al., 2017. Comparing direct observation of strain, rotation, and displacement with array estimates at Piñon Flat Observatory, California, *Seismol. Res. Lett.*, **88**(4), 1107–1116.
- Ekström, G., Nettles, M. & Dziewoński, A., 2012. The global CMT project 2004–2010: centroid-moment tensors for 13,017 earthquakes, *Phys. Earth planet. Inter.*, **200**, 1–9.
- Gutenberg, B. & Richter, C.F., 1936. On seismic waves (third paper), *Gelands Beitr. Geophys.*, **47**, 73–131.
- Hadjioannou, C., Nettles, M. & Dziewoński, A., 2012. The global CMT project 2004–2010: centroid-moment tensors for 13,017 earthquakes, *Phys. Earth planet. Inter.*, **200**, 1–9.
- Gutenberg, B. & Richter, C.F., 1936. On seismic waves (third paper), *Gelands Beitr. Geophys.*, **47**, 73–131.
- Hadjioannou, C., Gaebler, P., Schreiber, U., Wassermann, J. & Igel, H., 2012. Examining ambient noise using colocated measurements of rotational and translational motion, *J. Seismol.*, **16**(4), 787–796.
- Herak, M. & Herak, D., 1993. Distance dependence of Ms and calibrating function for 20 second Rayleigh waves, *Bull. seism. Soc. Am.*, **83**(6), 1881–1892.
- Igel, H., Cochard, A., Wassermann, J., Flaws, A., Schreiber, U., Velikoseltsev, A. & Pham Dinh, N., 2007. Broad-band observations of earthquake-induced rotational ground motions, *Geophys. J. Int.*, **168**(1), 182–196.
- Igel, H., Schreiber, U., Flaws, A., Schuberth, B., Velikoseltsev, A. & Cochard, A., 2005. Rotational motions induced by the M8.1 Tokachi-oki earthquake, September 25, 2003, *Geophys. Res. Lett.*, **32**(8), doi:10.1029/2004GL022336.
- Karnik, V., Kondorskaya, N., Riznichenko, J.V., Savarensky, E., Soloviev, S., Shebalin, N., Vanek, J. & Zatopek, A., 1962. Standardization of the earthquake magnitude scale, *Stud. Geophys. Geod.*, **6**(1), 41–48.
- Komatitsch, D. & Tromp, J., 2002a. Spectral-element simulations of global seismic wave propagation I. Validation, *Geophys. J. Int.*, **149**(2), 390–412.
- Komatitsch, D. & Tromp, J., 2002b. Spectral-element simulations of global seismic wave propagation II. Three-dimensional models, oceans, rotation and self-gravitation, *J. geophys. Int.*, **150**(1), 303–318.
- McLeod, D., Stedman, G., Webb, T. & Schreiber, U., 1998. Comparison of standard and ring laser rotational seismograms, *Bull. seism. Soc. Am.*, **88**(6), 1495–1503.
- Ritsema, J., Deuss, A., van Heijst, H.J. & Woodhouse, J.H., 2011. S40RTS: a degree-40 shear-velocity model for the mantle from new Rayleigh wave dispersion, teleseismic traveltimes and normal-mode splitting function measurements, *Geophys. J. Int.*, **184**(3), 1223–1236.
- Salvermoser, J. et al., 2017. An event database for rotational seismology, *Seismol. Res. Lett.*, **88**(3), 935–941.
- Sbaa, S., Hollender, F., Perron, V., Imtiaz, A., Bard, P.-Y., Mariscal, A., Cochard, A. & Dujardin, A., 2017. Analysis of rotation sensor data from the SINAPS@Kefalonia (Greece) post-seismic experiment—link to surface geology and wavefield characteristics, *Earth, Planets Space*, **69**(1), 124.
- Schreiber, K.U., Stedman, G.E., Igel, H. & Flaws, A., 2006a. Ring laser gyroscopes as rotation sensors for seismic wave studies, in *Earthquake Source Asymmetry, Structural Media and Rotation Effects*, pp. 377–390, Springer.
- Schreiber, U., Igel, H., Cochard, A., Velikoseltsev, A., Flaws, A., Schuberth, B., Drewitz, W. & Müller, F., 2006b. The GEOSensor project: rotations new observable for seismology, in *Observation of the Earth System from Space*, pp. 427–443, Springer.
- Shearer, P.M., 2009. *Introduction to Seismology*, Cambridge University Press.
- Sollberger, D., Greenhalgh, S.A., Schmelzbach, C., Van Renterghem, C. & Robertson, J.O., 2017. 6-C polarization analysis using point measurements of translational and rotational ground-motion: theory and applications, *Geophys. J. Int.*, **213**(1), 77–97.
- Soloviev, S.L., 1955. Classification of earthquakes in order of energy, *Trudy Geofiz. Inst. AN SSSR*, **30**(157), 3–31.
- Spudich, P., Steck, L.K., Hellweg, M., Fletcher, J. & Baker, L.M., 1995. Transient stresses at Parkfield, California, produced by the M 7.4 Landers earthquake of June 28, 1992: Observations from the UPSAR dense seismograph array, *J. geophys. Res.: Solid Earth*, **100**(B1), 675–690.
- Stedman, G., 1997. Ring-laser tests of fundamental physics and geophysics, *Rep. Prog. Phys.*, **60**(6), 615.
- Stein, S. & Wysession, M., 2009. *An Introduction to Seismology, Earthquakes, and Earth Structure*, John Wiley & Sons.
- Tanimoto, T., Hadjioannou, C., Igel, H., Wassermann, J., Schreiber, U., Gebauer, A. & Chow, B., 2016. Seasonal variations in the Rayleigh-to-Love wave ratio in the secondary microseism from colocated ring laser and seismograph, *J. geophys. Res.: Solid Earth*, **121**(4), 2447–2459.
- Vaněk, J., Zatopek, A., Karník, V., Kondorskaya, N.V., Riznichenko, Y.V., Savarensky, E.F., Solov'ev, S.L. & Shebalin, N.V., 1962. Standardization of magnitude scales, *Izv. Acad. Sci. G. Ser. USSR*, **2**, 108–111.

APPENDIX: TECHNICAL DETAILS

Since amplitude information and the resultant estimates of attenuation constants are heavily dependent on processing steps, we detail those here. All processing was done in Python (<https://www.python.org/>), with all data handling, preprocessing, filtering and manipulation accomplished using the seismology oriented Python toolbox, ObsPy (Beyreuther et al. 2010).

For each observation based magnitude scale, event and station information was gathered, including great circle distance (based on the Vincenty formula in the case of a spherical Earth), and theoretical backazimuth (based on a WGS84 ellipsoid with radius 6.378137E6 m and flattening of 3.353E-3 m). Event waveforms were downloaded via the FDSN (International Federation of Digital Seismograph Networks) web service, with a start time 180 s prior to the origin time of the event, and an end time 3 hr after the origin time of the event. Instrument response information was simultaneously fetched. Preprocessing steps in the following order were then performed: decimation to 1Hz sampling rate, de-mean, linear detrend (removing a simple linear regression line fit to the data), 5 per cent edge tapering, response removal (multiplication of the frequency domain response function with the fourier transform of the waveform; with a flat response between 120 s and 10 Hz), with a water level of 60 to prevent over amplification of small amplitudes. A 5 per cent edge taper was applied to the

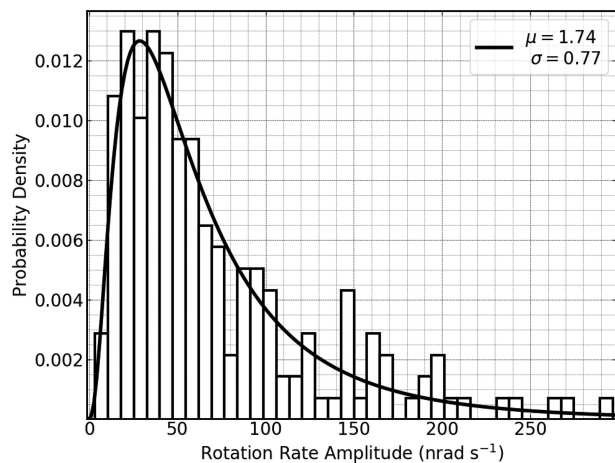


Figure A1. Histogram showing the logarithm of rotation rate amplitudes and a fitted log-normal probability density function. The relative log-normal distribution of amplitude measurements implies that a log-based linear regression is applicable for this data set. Translation data shows similar distribution.

final waveform. Waveforms were filtered with 4-corner Butterworth bandpass filters. Filters were run forward and back to avoid phase shifts.

To calculate peak values, maximum and minimum trace values and their corresponding locations were found. A search over 20 s around peak values was performed to locate the nearest and largest corresponding peak or trough. The vertical deflection be-

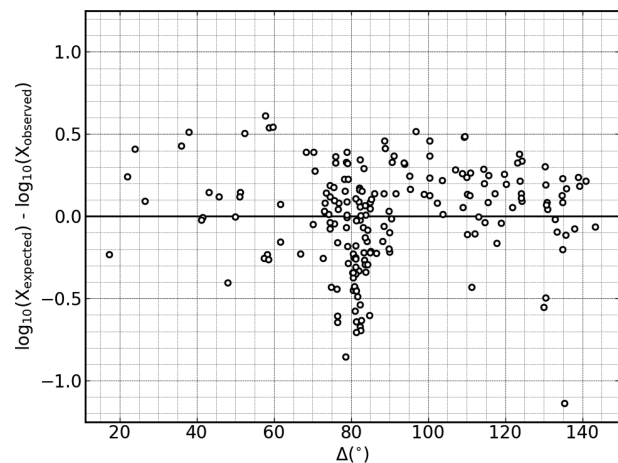


Figure A2. Residuals plotted against distance for measurements of peak rotation rate. The difference of the logarithm of expected rotation rate amplitudes and the logarithm of observed rotation rate amplitudes show random scatter when plotted over distance, indicating that a linear regression is suitable for this data set. Residual plots of other observables used in this study also show random scatter.

tween maximum peak and adjacent trough was found and divided by two, alongside the vertical distance between minimum trough and adjacent peak, divided by two. The larger of the two values was chosen as the ‘peak amplitude.’ Zero crossing was determined as the location of the zero between peak and trough, and the period was taken as two times the temporal distance between the location of the peak and trough.

Table A1. Translation magnitude scales for components and stations not presented in Table 2. Amplitude values for all scales given in nm s⁻¹. Values of C from Herak & Herak (1993) and Ambraseys & Free (1997) altered to give units in nm s⁻¹.

Scale	Label	B	C	Wave	N
Herak & Herak (1993)	M_s^{HH}	1.094	1.429	Rayleigh	–
Ambraseys & Free (1997)	M_s^{AF}	0.947	1.77	Rayleigh	–
Vertical velocity (FUR)	M_{ZV}^{FUR}	1.15 ± 0.33	1.02 ± 0.64	Rayleigh	189
Vertical velocity (PFO)	M_{ZV}^{PFO}	1.01 ± 0.25	1.48 ± 0.48	Rayleigh	194
Vertical velocity (ERM)	M_{ZV}^{ERM}	1.04 ± 0.09	1.24 ± 0.15	Rayleigh	188
Transverse velocity (WET)	M_{TV}^{WET}	1.35 ± 0.33	0.75 ± 0.63	Love	195
Transverse velocity (FUR)	M_{TV}^{FUR}	1.46 ± 0.31	0.44 ± 0.61	Love	191
Transverse acceleration (WET)	M_{TA}^{WET}	1.79 ± 0.28	0.33 ± 0.55	Love	195
Synthetic transverse velocity	M_{TV}^{SYN}	0.94 ± 0.11	0.94 ± 0.22	Love	571